

Magnified or multiply imaged? – Search strategies for gravitationally lensed supernovae in wide-field surveys

Radosław Wojtak¹,^{*} Jens Hjorth and Christa Gall

DARK, Niels Bohr Institute, University of Copenhagen, Lyngbyvej 2, DK-2100 Copenhagen, Denmark

Accepted 2019 May 24. Received 2019 May 21; in original form 2019 March 18

ABSTRACT

Strongly lensed supernovae (SNe) can be detected as multiply imaged or highly magnified transients. In order to compare the performances of these two observational strategies, we calculate expected discovery rates as a function of survey depth in five *grizy* filters and for different classes of SNe (types Ia, IIP, IIL, Ibc, and IIn). We find that detections via magnification is the only effective strategy for relatively shallow pre-LSST (Large Synoptic Sky Survey) surveys. For survey depths about the LSST capacity, both strategies yield comparable numbers of lensed SNe. SN samples from the two methods are to a large extent independent and combining them increases detection rates by about 50 percent. While the number of lensed SNe detectable via magnification saturates at the limiting magnitudes of LSST, detection rates of multiply imaged SN still go up drastically at increasing survey depth. Comparing potential discovery spaces, we find that lensed SNe found via image multiplicity exhibit longer time delays and larger image separations making them more suitable for cosmological constraints than their counterparts found via magnification. We provide useful fitting functions approximating the computed discovery rates for different SN classes and detection methods. We find that the Zwicky Transient Factory will find about two type Ia and four core-collapse lensed SNe per year at a limiting magnitude of 20.6 in the *r* band. Applying a hybrid method which combines searching for highly magnified or multiply imaged transients, we find that LSST will detect 89 type Ia and 254 core-collapse lensed SNe per year. In all cases, lensed core-collapsed SNe will be dominated by type IIn SNe contributing to 80 per cent of the total counts, although this prediction relies quite strongly on the adopted spectral templates for this class of SNe. Revisiting the case of the lensed SN iPTF16geu, we find that it is consistent within the 2σ contours of predicted redshifts and magnifications for the intermediate Palomar Transient Factory survey.

Key words: gravitational lensing: strong – methods: statistical – supernovae: general.

1 INTRODUCTION

The phenomenon of strongly lensed (multiply imaged) supernovae (SNe) has long been theoretically considered (Refsdal 1964), but the first detections became possible only very recently. Quimby et al. (2014) found a strongly lensed Type Ia SN magnified by a factor of 30, although multiple images were not resolved. The first fully resolved image configuration of a lensed supernova was reported by Kelly et al. (2015). The SN (SN Refsdal) was a core-collapse type (Kelly et al. 2016) and lensed by an intervening galaxy cluster and a massive galaxy in the cluster. The second example of a fully resolved lensed SN was iPTF16geu (Goobar et al. 2017). Detected as an exceptionally luminous SN (for its redshift) in a

regular transient survey, the intermediate Palomar Transient Factory (iPTF), it was subsequently observed by ESO Very Large Telescope (VLT), Keck Observatory, and the *Hubble Space Telescope* (HST) whose images revealed a quadrupole lensing configuration with a subarcsecond scale of image separations. The SN was classified as a type Ia SN (Goobar et al. 2017; Cano et al. 2018). High-cadence imaging of massive galaxy clusters with *HST* also recently resulted in the discovery of a new type of lensed transients which appeared to be strongly lensed individual stars (Rodney et al. 2018; Kelly et al. 2018; Chen et al. 2019; Kaurov et al. 2019).

Strongly lensed SNe are unique objects in several respects, making them a promising tool for constraining cosmological parameters such as the Hubble constant (Grillo et al. 2018; Vega-Ferrero et al. 2018). With well-studied light curves, reasonably well represented by simple models, lensed SNe appear to be suitable for precise measurements of time delays from even relatively short observing

* E-mail: radek.wojtak@nbi.ku.dk

campaigns (Rodney et al. 2016). If, in addition, a lensed SN is of Type Ia, extra constraints from the standard candle nature come into play. This can be used to measure magnification in an independent way (Rodney et al. 2015) and thus provide additional constraints on the lens model. This extra information can potentially narrow down inherent degeneracies in lens models which leave all lensing observables invariant, except the time delay (Schneider & Sluse 2014). The unresolved degeneracies are the main source of potential systematic errors in cosmological constraints obtained from time-delay observations (Kolatt & Bartelmann 1998; Oguri & Kawano 2003).

Strongly lensed supernovae will be found in large numbers and in a more automatic way in ongoing and future transient surveys (see e.g. Diego 2018). Two possible strategies for finding plausible candidates can be considered. One can search for multiply imaged supernovae (Oguri & Marshall 2010) or highly magnified (unresolved) transients (Goldstein & Nugent 2017). The former probes a unique feature indicating unambiguously the lensing nature of a candidate. The latter approach is less direct and involves an estimate of how much brighter an observed supernova is compared to a fiducial reference supernova, as it would have been observed in the lens galaxy (or the apparent host galaxy). Atypically bright supernovae in this case would indicate a high chance of observing a higher redshift, gravitationally magnified (amplified) supernova.

Searching for lensed supernovae via image multiplicity or magnification are the main observational strategies based on two characteristic features of the lensing phenomenon. The expected discovery rates have been estimated in several studies; however, each of them considering only one of the two methods and adopting specifications of upcoming surveys (Oguri & Marshall 2010; Goldstein & Nugent 2017; Goldstein, Nugent & Goobar 2018a). At present, it is unclear to what extent the two methods are equivalent or complementary, which technique is more effective in finding lensed SNe in different ranges of limiting magnitudes or whether one would benefit from combining them. The two methods may differ not only in terms of their performance in finding candidates, but also in terms of the characteristics of the resulting lensed SN samples. This in turn raises the question which SN sample and thus which method would be suitable for robust measurements of time delays for the purpose of cosmological inference. In order to address these issues, we compute detection rates for both methods and a wide range of possible filters and SN types. This allows us to make the first comprehensive comparison of detection methods in terms of the discovery potential and the cosmological constraining power of the expected gravitationally lensed SN samples. We explore the possibilities of boosting discovery rates by combining the methods and we revisit the estimates of detections rates for ongoing and upcoming transient surveys.

Estimating discovery rates of gravitationally lensed supernovae is not merely a means for quantifying the efficiency of detection methods. Lensed SNe can be also regarded as a cosmological tool probing a wide range of physical properties across cosmic time, e.g. volumetric rates and luminosity functions of SNe, lens models, or cosmological parameters. Observed detection rates can potentially shed light on some aspects of our current models.

The paper is organized as follows. Section 2 outlines detection methods and the potential of increasing their discovery potential by combining them. We describe the computation of discovery rates as well as the underlying lens model and volumetric supernova rates in Section 3. The results are presented in Section 4 followed by a discussion in Section 5 and concluding remarks in Section 6. We adopt a flat Λ CDM (Λ cold dark matter) cosmological model with $\Omega_m = 0.3$ and $H_0 = 73 \text{ km s}^{-1} \text{ Mpc}^{-1}$.

2 OBSERVATIONAL STRATEGIES

The two main features through which strong lensing manifests itself are the multiplicity of images and the magnification of each image. Therefore, strongly lensed SNe can be detected and distinguished from ordinary non-lensed SNe if they appear as spatially and temporarily coincident transients (Oguri & Marshall 2010) or exceptionally bright transients (Goldstein & Nugent 2017). In the following, we outline each observational strategy and the related detection criteria in more detail.

2.1 Image multiplicity

The critical factors for detecting multiple images are the image separations relative to the seeing, the flux contrast between the images, and the apparent magnitudes of the faintest images in the configuration. As a base model for this strategy, we adopt detection criteria optimized for the Large Synoptic Sky Survey (LSST), as proposed by Oguri & Marshall (2010). Following this approach, a transient is identified as a strongly lensed supernova if (i) the maximum image separation θ_{\max} between images falls into a range between 0.5 and 4 arcsec, where these limits stem from seeing conditions as well as the choice of selecting systems lensed by isolated galaxies, characterized by relatively simple lens models, (ii) the flux ratio between the images for doubly imaged supernovae is larger than 0.1 and (iii) at least three or two images are detected for quads/cusps (four/three images) and doubles (two images), respectively. For sufficiently bright SNe and a suitable survey cadence, this strategy not only yields detections of multiply imaged SNe, but it also enables the measurement of basic lensing properties such as time delays and flux ratios between the images. In this respect, this is an ideal observational strategy for large and self-contained surveys such as the LSST. Initial information on lensing configurations can be also used to pin down the best candidates for follow-up observations.

2.2 Magnification

Strongly lensed supernovae can be detected as transients which appear significantly brighter than the brightest supernovae at the redshift of the apparent host galaxy (lens galaxy for lensed supernovae or actual host galaxy for non-lensed transients). Following Goldstein & Nugent (2017), the detection criterion can be formulated in the following way:

$$m_X(t_{\text{peak}}) < \langle M_X \rangle(t_{\text{peak}}) + \mu(z_{\text{host}}) + K_{XX}(z_{\text{host}}, t_{\text{peak}}) + \Delta m, \quad (1)$$

where $m_X(t_{\text{peak}})$ is the observed peak magnitude of the transient in band X , $\langle M_X \rangle(t_{\text{peak}})$ is a mean absolute magnitude of a reference class of brightest SNe in band X at peak, μ is the distance modulus, z_{host} is redshift of the apparent host galaxy, $K_{XX}(z_{\text{host}}, t_{\text{peak}})$ is a K -correction for the assumed reference class of brightest supernovae at the peak of their light curves and $\Delta m < 0$ is a free parameter defining the magnitude gap between lensed and non-lensed supernovae. Absolute magnitudes and K -corrections can be calculated from spectral templates of the assumed reference class of bright SNe, while the redshift of the apparent host galaxy can be estimated from existing photometric data from wide-field surveys. Since only rare cases of SNe are brighter than SNe Ia, e.g. superluminous SNe, it is reasonable to use type Ia as the reference class of bright SNe. Like Goldstein & Nugent (2017), we assume a mean peak absolute magnitude of -19.3 in the B band.

The choice of the parameter Δm is dictated by a trade-off between the completeness and the contamination of the selected lensed SN candidates. As a base model, we use $\Delta m = -0.7$ required for distinguishing between the brightest non-lensed type Ia SNe and gravitationally lensed SNe (Goldstein & Nugent 2017). We expect that the assumed magnitude gap is a sufficiently conservative choice from the point of view of minimizing the false positive rate. However, one has to bear in mind that rare luminous SNe brighter than -20 in the B band inevitably will be confused with lensed SNe in this approach.

The effective depth of a transient survey in the context of detecting strongly lensed SNe via magnification is modulated by the extent to which all lensing images contribute to the measured flux. It is natural to consider here two scenarios in which the total observed flux either comes from all images or is simply approximated by the flux of the brightest image. The former, which we adopt as our base model, sets an upper limit on the effective depth and discovery rates with respect to how efficiently the measured flux is integrated over all images. The latter determines the corresponding lower limits. We expect that most realistic detections in typical transient surveys will be intermediate between the two extremes.

Compared to the strategy based on detection of multiple images, the competitiveness of this method heavily relies on follow-up observations. Higher resolution and deeper observations are necessary to both confirm the lensing nature of the candidates (by means of detecting multiple images) and determining the lensing configuration.

Although initially envisaged for finding strongly lensed type Ia SNe, the method can be also applied to detecting gravitationally lensed core-collapse SNe (Goldstein et al. 2018a). Here, using type Ia SNe as the reference class of bright SNe sets a relatively conservative detection threshold. However, as we shall see, the higher volumetric rates of core-collapse SNe can compensate their lower luminosities leading to even higher discovery rates than for type Ia.

2.3 Hybrid approach

As we shall see in Section 4, the two methods described perform very differently. The methods are complementary in many respects in that they maximize their efficiencies in different ranges of survey depth. This provides motivation for considering a third approach which combines the ideas underlying the two techniques. Here, a transient is classified as a lensed SN candidate if at least one of the two methods identifies it as a potential lensed SN.

3 SIMULATIONS

We employ a Monte Carlo approach to compute the expected number of observed strongly lensed SNe. The method relies on drawing random realizations of lens galaxies and SNe in a light-cone, and counting strong lensing events which satisfy certain detection conditions.

3.1 Lens galaxies

Motivated by its success in modelling multiply imaged QSOs, we assume that the mass distribution in the lens galaxies is adequately represented by a Singular Isothermal Ellipsoid model (Kormann, Schneider & Bartelmann 1994) in which the convergence κ is

given by:

$$\kappa(x, y) = \frac{\theta_E}{2} \frac{\lambda(e)}{\sqrt{(1-e)^{-1}x^2 + (1-e)y^2}}, \quad (2)$$

$$\theta_E = 4\pi \left(\frac{\sigma}{c} \right)^2 \frac{D_{ls}}{D_s}, \quad (3)$$

where θ_E is the Einstein radius, σ is the line-of-sight velocity dispersion of the lens galaxy, D_s and D_{ls} are angular diameter distances, respectively, between the observer and the source, and the lens galaxy and the source. The convergence depends on the shape of the lens galaxy through the ellipticity e of the projected lensing mass surface density, which includes the contributions from dark matter and baryonic components, both relevant for the statistics of strong lensing images (Castro et al. 2018). We assume that the ellipticity is given by the light distribution. Based on observational constraints, we adopt a Gaussian distribution for the ellipticity with a mean of 0.3 and dispersion of 0.16, with a truncation at 0.1 and 0.9 (Oguri et al. 2008). The function $\lambda(e)$ is the so-called dynamical normalization and it depends on the deprojected shape of the lens galaxy. Following Chae (2003), we assume that both oblate and prolate ellipsoids approximate the actual shapes of lens galaxies with equal probabilities, implying $\lambda(e) \approx 1$.

In order to make the simulated lensing more realistic, we account for the effect of the lens environment by including external shear (Kochanek 1991; Witt & Mao 1997; Keeton, Kochanek & Seljak 1997) with a potential given by

$$V(x, y) = \frac{\gamma}{2} (x^2 - y^2) \cos(2\theta_\gamma) + \gamma xy \sin(2\theta_\gamma), \quad (4)$$

where γ is the magnitude of the external shear and θ_γ is its position angle on the image plane. We assume that γ follows a lognormal distribution with mean 0.05 and dispersion 0.2 dex, as expected for the external shear around early-type galaxies, calculated by ray tracing in cosmological simulations of the standard cosmological model (Holder & Schechter 2003). We expect that the employed simulation-based calibration of the external shear to a large extent accounts for lensing effects from realistic structures around lens elliptical galaxies, although the presence of a galaxy cluster may in addition affect the image configuration. The external shear in our model is uncorrelated with the orientation of the lens galaxy, i.e. it has a random orientation in the image plane.

We model the mass function of lens galaxies in terms of the velocity dispersion function of early-type galaxies, which are most common lens galaxies. The velocity dispersion function is well approximated by a modified Schechter function of the following form:

$$\frac{dn}{d\sigma} = \phi_* \left(\frac{\sigma}{\sigma_*} \right)^\alpha \exp \left[- \left(\frac{\sigma}{\sigma_*} \right)^\beta \right] \frac{\beta}{\Gamma(\alpha/\beta)} \frac{1}{\sigma}, \quad (5)$$

where n is the comoving density of galaxies. We use the above probability density to draw random realizations of lens galaxies in our calculations. We adopt parameters derived from fitting this model to the Sloan Digital Sky Survey (SDSS) data (Choi, Park & Vogeley 2007), i.e.

$$\begin{aligned} \phi_* &= 8.0 \times 10^{-3} h^3 \text{Mpc}^{-3} \\ \sigma_* &= 161 \text{ km s}^{-1} \\ \alpha &= 2.32 \\ \beta &= 2.67. \end{aligned} \quad (6)$$

Following Goldstein & Nugent (2017), we narrow the range of velocity dispersions to (50 and 400 km s⁻¹) for galaxies which can

effectively act as gravitational lenses. The lower limit coincides also with the minimum velocity dispersion measured from the SDSS spectroscopic observations.

We assume that the velocity dispersion function does not evolve with redshift. Although observational constraints on the velocity dispersion function are limited at high redshifts, this assumption is corroborated by existing data showing no evidence of redshift evolution at $z \lesssim 1$, especially for the high velocity dispersion tail (Bezanson et al. 2011; Montero-Dorta, Bolton & Shu 2017). The assumption is also supported by theoretical arguments based on the standard model for halo formation, for which Mitchell et al. (2005) showed that the normalization of the velocity dispersion function can be higher only by ~ 15 per cent at redshift $z = 1$, at which only rare galaxies can generate strongly lensed images of high-redshift SNe detectable in surveys with depths comparable to the LSST.

The number of lens galaxies in an observational cone as a function of redshift and velocity dispersion is given by

$$\frac{dN_{\text{lens}}}{d\sigma dz} = 4\pi \frac{c}{H_0} \frac{(1+z)^2 D_A^2}{E(z)} \phi(\sigma), \quad (7)$$

where D_A is the angular diameter distance, and $E(z) = H(z)/H_0$ is the dimensionless Hubble parameter. We note that the simulated redshift distribution of lens galaxies is independent of the Hubble constant adopted in our work and the only role of the assumed cosmological model is to extrapolate the redshift distribution from the redshifts of the main galaxy sample in the SDSS to higher redshifts.

3.2 Supernovae

The total number of observed SNe per unit time as a function of redshift is given by

$$\frac{dN_{\text{SN}}}{dz} = 4\pi \frac{c}{H_0} \frac{(1+z)^2 D_A^2}{E(z)} \frac{1}{1+z} n_{\text{SN}}(z), \quad (8)$$

where $n_{\text{SN}}(z)$ is the volumetric SN rate in a local rest frame. Compared to equation (7), the additional factor $1/(1+z)$ accounts for a conversion from a local to the observer rest frame.

We compute the volumetric type Ia SN rate as the convolution of the delay time distribution $\text{DTD}(t)$ with the star formation history $\psi(t)$, i.e.

$$n_{\text{SNIa}}(t) = \int_0^t \psi(t-\tau) \text{DTD}(\tau) d\tau. \quad (9)$$

For the star formation history, we employ a model from Madau & Dickinson (2014), based on a compilation of the cosmic star formation rates determined from ultraviolet (UV) and infrared (IR) observations:

$$\psi(z) = 0.015 \frac{(1+z)^{2.7}}{1 + [(1+z)/2.9]^{5.6}} \text{M}_\odot \text{yr}^{-1} h_{70} \text{Mpc}^{-3}. \quad (10)$$

Following Rodney et al. (2014), we assume that the delay time distribution is accurately described by the following piecewise function:

$$\text{DTD}(t) = \begin{cases} 0 & \text{if } t < 0.04 \text{ Gyr} \\ \eta_1 & \text{if } 0.5 \text{ Gyr} < t < 0.04 \text{ Gyr} \\ \eta_0 t^{-1} & \text{if } t > 0.5 \text{ Gyr} \end{cases} \quad (11)$$

where η_0 and η_1 are free parameters. This model is well motivated by observations (Rodney et al. 2014; Andersen & Hjorth 2018) as well as theoretical arguments derived from the evolution of binary systems (Maoz & Mannucci 2012). It accounts both for

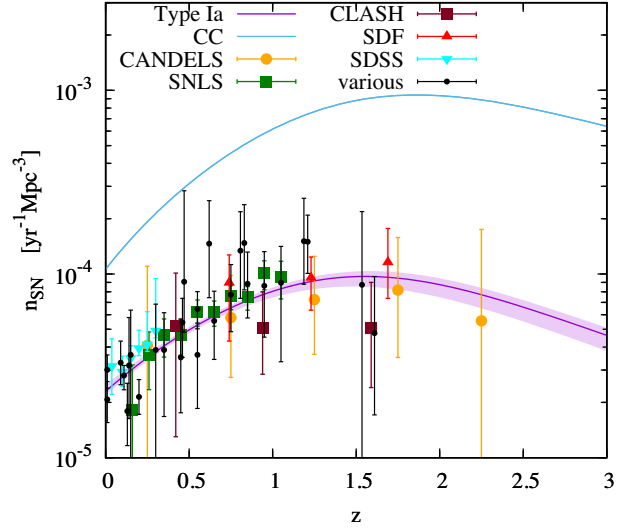


Figure 1. Comoving volumetric rate of type Ia and core-collapse SNe assumed in our study. For core-collapse type, the rate is given by the star formation history from Madau & Dickinson (2014); for type Ia, the rate is the convolution of a delay time distribution given by equation (11) with the adopted model of star formation history. Data points show observational measurements of the rate for type Ia, as compiled by Graur et al. (2014). The various distinct symbols highlight selected results from CANDELS (Rodney et al. 2014), the Supernova Legacy Survey (Perrett et al. 2012), the Cluster Lensing And Supernova survey with Hubble (Graur et al. 2014), the Subaru Deep Field (Graur et al. 2011) and the SDSS (Dilday et al. 2010). Black symbols include results from Graur & Maoz (2013), Barbary et al. (2012), Melinder et al. (2012), Li et al. (2011), Rodney & Tonry (2010), Botticella et al. (2008), Dahlen, Strolger & Riess (2008), Dilday et al. (2008), Horesh et al. (2008), Blanc et al. (2004), Tonry et al. (2003), Pain et al. (2002), Hardin et al. (2000), and Cappellaro, Evans & Turatto (1999).

the population of prompt SNe with delay time $t < 0.5$ Gyr (with 40 Myr as the shortest possible time before explosion, Belczynski, Bulik & Ruiter 2005) and delayed supernovae with $\text{DTD} \propto t^{-1}$ and $t > 0.5$ Gyr. The two free parameters can be determined by fitting the model to the rates inferred from observations. We carry out the fit using a compilation of observational determinations of the volumetric type Ia SN rates from Graur et al. (2014) updated with the results from the Cosmic Assembly Near-infrared Deep Extragalactic Legacy Survey (CANDELS; Rodney et al. 2014). Minimization of χ^2 with errors including statistical and systematic uncertainties yields $\eta_0 = 1.02^{+0.27}_{-0.15} \times 10^{-4} h_{70}^2 \text{yr}^{-1} \text{M}_\odot^{-1}$ and $\eta_1/\eta_0 = 11.98^{+3.37}_{-4.49}$. Fig. 1 compares the resulting best-fitting model to the observational data. The obtained constraints imply a fraction of prompt supernovae $f_p = 0.63^{+0.07}_{-0.11}$, consistent with the results obtained by Rodney et al. (2014).

The rate of core-collapse SNe is directly proportional to the star formation history $\psi(z)$:

$$n_{\text{SNCC}}(z) = k_{\text{CC}} \psi(z), \quad (12)$$

where k_{CC} is the number of stars that explode as SNe per unit mass. For our study, we adopt $k_{\text{CC}} = 0.0068 \text{M}_\odot^{-1}$ expected for a mass range of SN progenitors (8, 40 M_\odot) and a Salpeter initial mass function. Since the same initial function was consistently assumed in the derivation of the star formation rate from observations, the predicted rate of core-collapse SNe is practically independent of the initial mass function (Madau & Dickinson 2014). The resulting core-collapse SN rate is shown in Fig. 1.

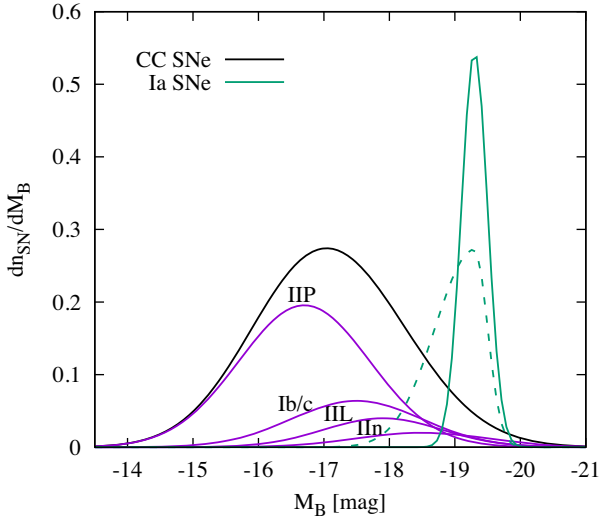


Figure 2. Distribution of absolute luminosities in the B band of the different types of SNe considered in our study. Normalizations of the distributions are proportional to the local volumetric rates of the corresponding SN classes. The green dashed curve shows an alternative model for type Ia SNe with a tail accounting for low-luminosity SNe.

We calculate light curves and K -corrections of simulated type Ia SNe (normal branch) using a time-series of spectral templates computed by Nugent, Kim & Perlmutter (2002). Following Goldstein & Nugent (2017), we assume that the absolute magnitude is normally distributed with a mean of -19.3 in the B band and a scatter of 0.2 . We also check the impact of using a more realistic distribution with three times longer Gaussian tail at low luminosities accounting for faint supernovae in volume-limited samples (see e.g. Li et al. 2011; Goldstein & Nugent 2017). For core-collapse SNe, we consider types Ib/c, IIP, IIL, and IIn, assuming that their relative contributions to the total number density of core-collapse SNe are independent of redshift and constrained by low-redshift observations resulting in 16, 49, 9, and 5 per cent respectively for Ib/c, IIP, IIL, and IIn (Li et al. 2011; Graur et al. 2017). We realize light curves of the four SN subclasses using spectral templates from a compilation which is an extension of the work by Nugent et al. (2002),¹ based primarily on data from Levan et al. (2005) for type Ib/c, Di Carlo et al. (2002) for IIn, and Gilliland, Nugent & Phillips (1999) for the remaining two types. We approximate the distribution of absolute magnitudes in the B band by Gaussians with mean and scatter of -17.50 and 1.0 for type Ib/c, -16.70 and 1.0 for type IIP, -17.9 and 0.90 for type IIL, -18.5 and 1.0 (after discarding two outliers with $M_B = -15.1, -22.2$) for IIn (Richardson et al. 2014a, for $h = 0.73$). The assumed luminosity functions for all classes of SNe are shown in Fig. 2. We note that the borderline between different classes may not be entirely clear cut. For example, there may be a continuous transition between type IIP and type IIL SNe (e.g. Anderson et al. 2014). In this sense, these types can be seen as being representative for the fainter and more luminous ends of the type II SN population.

3.3 Computation

First, we generate a random sample of lens galaxies at redshifts $z < 1.2$. We find that it is sufficient to realize 10^5 lens galaxies

and then rescale the final counts of strongly lensed SNe according to the actual number of lens galaxies contained in the assumed comoving volume. Then, we populate the observational cone up to redshift $z = 3$ with SNe. In order to reduce shot noise, we artificially increase the SNe rate by a factor of 5×10^5 . The actual detection rate is then retrieved by scaling down the counts by the same factor. In order to save computational time (driven primarily by lensing computations), we discard all supernovae at angular distances larger than $4\theta_E$. These SNe are typically too far from the lenses to be multiply imaged or strongly magnified. Our choice of a maximum redshift for the lenses and the SNe allows us to determine detection rates of strongly lensed SNe for limiting magnitudes up to 26, which is around 2 mag deeper than the envisaged depth for the LSST.

For every lens–supernova pair we calculate all basic lensing properties, i.e. image multiplicity, magnifications, positions of the images, and time delays. The lensing equations are solved numerically using the publicly available code for lensing calculations, GLAFIC (Oguri 2010). When calculating time-dependent apparent magnitudes, we take into account both the effects of magnification and time delay determined for every image.

Once the complete Monte Carlo sample of strongly lensed SNe is computed, we can employ different detection criteria and thus determine the number of detectable lensed SNe as a function of survey depth in several different bands. This part of the calculations is independent of the assumed cosmological model and volumetric SN rates; therefore, it can be repeated for different detection criteria using the same pre-computed Monte Carlo sample of strongly lensed SNe and the corresponding lensing properties. The SN yields are computed for observations in five SDSS/LSST filters: g , r , i , z , and y .

4 RESULTS

4.1 Type Ia supernovae

Fig. 3 compares detection rates for strongly lensed type Ia SNe expected for the three methods with the base choice of free parameters, as outlined in Section 2. Our results demonstrate that the method based on detecting highly magnified SNe surpasses the image multiplicity technique for relatively shallow surveys with limiting magnitudes $\lesssim 22$. In particular, for a survey with a 21 mag depth, the magnification method is expected to find ~ 20 times more strongly lensed SNe than the image multiplicity method. Due to the stronger dependence on the limiting magnitude for the image multiplicity method, this ratio becomes larger for even shallower surveys, with a threefold change per magnitude in the i band.

For limiting magnitudes $\gtrsim 23$, increasing survey depth does not improve the performance of the magnification method, but it appreciably increases the rates for the other method. For deep surveys like the LSST, detecting multiple images appears to become a more powerful means for finding lensed type Ia SNe than gravitational magnification. The image multiplicity method is expected to yield about twice as many detections as the magnification method at a limiting magnitude of 24. The difference between the two methods becomes even more prominent for deeper surveys: the rates expected for the image multiplicity method increase exponentially with limiting magnitudes in a range between 24 and 26, whereas the rates from the magnification method become constant.

Both methods are expected to find comparable numbers of lensed type Ia SNe at limiting magnitudes between 23.0 in the g band to 23.8 in the y band. The lensed SN samples returned by the two methods happen to be only weakly overlapping; therefore,

¹https://c3.lbl.gov/nugent/nugent_templates.html

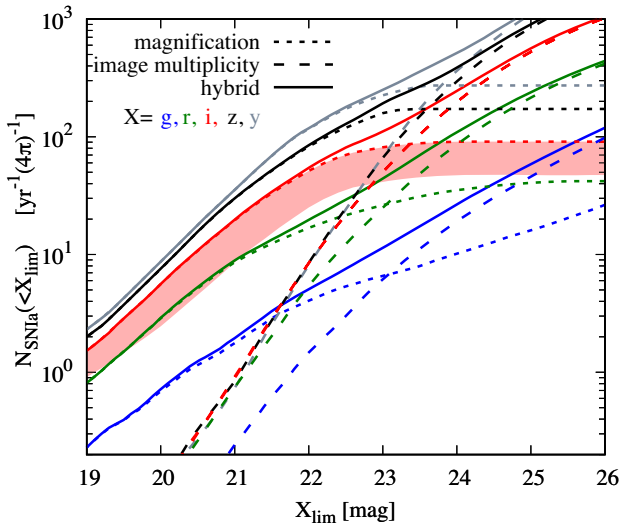


Figure 3. Detection rates of strongly lensed type Ia SNe as a function of survey depth in five different bands, in an all-sky search. The long- and short-dashed curves compare the SNe yields expected for two different observational strategies based on detecting image multiplicity or highly magnified SNe. The solid curves show the yields for the hybrid method which maximizes detection rates by means of combining both detection criteria. The shaded band indicates the range of detection rates given by the extent to which flux is integrated over the SN images, with the upper and lower limits corresponding to the total measured flux from all images (upper limit) or solely from the brightest image (lower limit).

combining both detection criteria is expected to increase the yields, especially at intermediate limiting magnitudes. This is demonstrated by the solid curves which show detection rates for the hybrid method which identifies strongly lensed SNe either as highly magnified or multiply imaged transients. The hybrid method maximizes SN yields at all limiting magnitudes. Unsurprisingly, it follows closely the rates from the magnification method at $X_{\text{lim}} \lesssim 21$ and the image multiplicity technique at $X_{\text{lim}} \gtrsim 24$.

The performance of the magnification method depends on the choice of the number of images that contribute to the total flux in the observations. The red band in Fig. 3 shows the expected range of the rates modulated by this effect. The upper limit corresponds to detections based on flux integrated over all images, whereas the lower limit is expected for detections based on flux solely from the brightest image. The average ratio between the upper and lower limits is 2, with a very weak dependence on survey depth and filters.

The apparent differences between detection rates from the two main methods reflect the fact that gravitational magnification and image multiplicity are not equally prominent features of strong lensing at different depths. The relatively poor performances of the magnification method for deep surveys ($X_{\text{lim}} > 23$) or the image multiplicity method for shallower surveys ($X_{\text{lim}} < 23$) cannot be appreciably improved by modifying the criteria for selecting the candidates. We demonstrate these intrinsic limitations in Fig. 4, where we show supernova yields for different choices of the free parameters defining the detection criteria in the two methods. Reducing the magnitude gap Δm in the magnification method results naturally in a higher detection rate. However, the improvement is limited solely to magnitudes $\gtrsim 22$ where the method is clearly outperformed by the image multiplicity technique. Furthermore, this inevitably leads to a higher false positive detection rates due to intrinsically bright type Ia SNe.

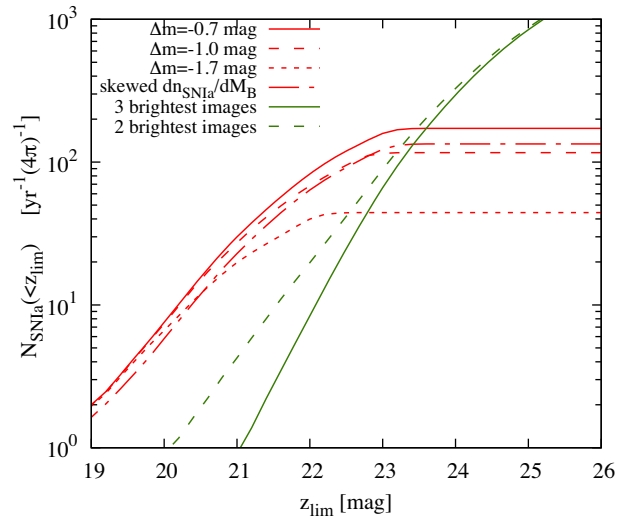


Figure 4. Sensitivity of detecting lensed type Ia SN in the z band to parameters and conditions defining detection criteria of the two methods based on selecting highly magnified (red curves) or multiply imaged supernovae (green curves). The parameter Δm is a minimum enhancement of the apparent brightness due to lensing magnification relative to the mean magnitude of type Ia SNe expected in the apparent host (lens) galaxy ($\Delta m = -0.7$ for the base model). For the image multiplicity method, discovery rates depend on the minimum number of detectable images. The solid and dashed curves compare the two cases for which at least three (base model) or two images are detectable for quads and cusps. The red dashed-dotted curves shows the impact of accounting for the possible low-luminosity tail in the luminosity function dn_{SNIa}/dM_B of type Ia SNe (see the green dashed curve in Fig. 2) on the expected discovery rates.

Relaxing the selection criteria for the image multiplicity method by including all systems with at least two detectable images (for all images configurations) improves the SN yields only at small limiting magnitudes, e.g. by a factor of 4 at $z_{\text{lim}} \approx 21$ (see the green dashed curve in Fig. 4). The resulting detection rates, however, are still smaller than those of the magnification method. Since the selection criterion cannot be relaxed even further, this case sets an upper limit for the expected detection rates based on image multiplicity. Finally, we find that changing the range of the maximum image separation does not appreciably modify the predictions for the lensed supernova yields.

A strong limitation of the magnification method is reflected by a plateau at $X_{\text{lim}} \gtrsim 22.5$ which signifies that the method does not benefit from increasing survey depth. This feature is an unavoidable drawback of the method and it cannot be removed by simply adjusting Δm (subject to a reasonable condition $\Delta m < 0$). It is primarily caused by the fact that high-redshift lenses and SNe require extremely large, and therefore improbable, magnifications in order to fall within a range of detectable fluxes. We illustrate this in Fig. 5 which compares selections of lensed SN candidates in shallow ($i_{\text{lim}} = 21$) and deep ($i_{\text{lim}} = 25$) surveys. Faint, high-redshift SNe are not sufficiently magnified in order to be selected by the magnification method. Most of them happen to be fainter than a fiducial reference type Ia SN with absolute luminosity $M_B = -20$ that would be observed in the apparent host galaxy (actual lens galaxy). On the other hand, faint SNe from deep surveys appear to exhibit relatively brighter secondary images than those from shallow surveys. This makes the image multiplicity method more effective in selecting lensed SN candidates in deep surveys at $X_{\text{lim}} \gtrsim 23.5$.

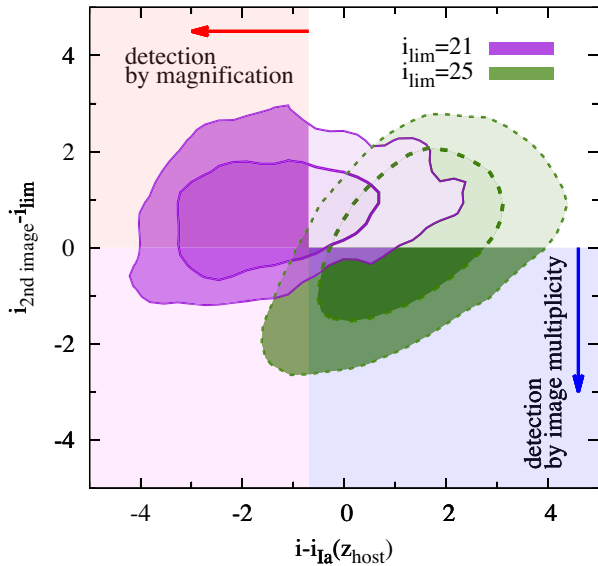


Figure 5. Selection of lensed SN candidates (using type Ia as an example) by means of finding highly magnified transients, i.e. brighter than a fiducial type Ia SNe observable in the apparent host (actual lens) galaxy (see the red arrow and the indicated shaded region), or detecting the second brightest image (see the blue arrow and the indicated shaded region). The two contours show the distribution of all observable lensed SNe in two surveys with depths of 21 and 25 in the i band. The majority of bright, low-redshift SNe appear to be highly magnified, but featuring the secondary image beyond detection limits (purple contours). They can be found using primarily the magnification method. On the other hand, the majority of faint, high-redshift lensed SNe from a deep survey (green contours) are not sufficiently magnified to be detected as peculiarly bright supernovae, but they exhibit detectable second brightest images. These lensed SNe can be effectively found as doubly imaged transients.

In order to show more quantitatively the differences between the magnification and image multiplicity methods of selecting lensed SNe candidates, we calculate the completeness of lensed SN searches as a function of survey depth (see Fig. 6). We define the 100 percent complete reference sample as consisting of all observable/detectable lensed type Ia SNe, i.e. all multiply imaged type Ia SNe that are brighter than X_{lim} at the peak of their light curves in at least one of the five bands, where apparent magnitudes are computed by integrating flux over all images. The figure shows that the magnification method maximizes its completeness for shallow surveys, with completeness reaching 80 percent at $\lesssim 21.5$ mag in the z or y band, and then it degrades at large survey depths. An inverse trend characterizes the completeness of the image multiplicity method which becomes more complete with increasing survey depth, reaching about 40 percent at 25 mag in the y or z bands. The solid curves show the completeness of the hybrid method. It is evident that combining the magnification and the image multiplicity detection criteria improves the completeness at limiting magnitudes characteristic for the LSST, i.e. $22 < X_{\text{lim}} < 24$. In particular, the hybrid method boosts the completeness by about 50 percent in the y band relative to lensed SN searches based solely on the magnification or image multiplicity criterion. Fig. 7 demonstrates also a difference between the magnification and image multiplicity methods in terms of redshift completeness. While the magnification technique can never be more complete than 20 percent at all redshifts, the image multiplicity method attains an 80–90 percent completeness up to a maximum redshift set by the survey depth.

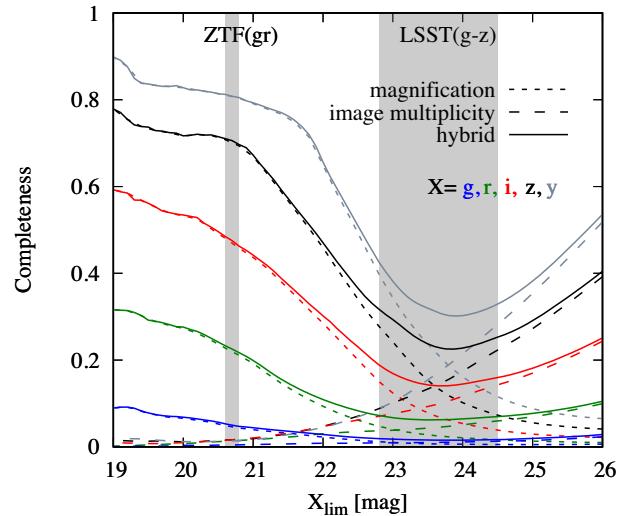


Figure 6. Completeness of lensed SN candidates found with three different methods, as a function of survey depth in five different bands. The vertical grey bands indicate the depths of ZTF and LSST. The method based on detecting highly magnified supernovae reaches an ~ 80 percent completeness in the z and y bands at $X_{\text{lim}} < 21$. The completeness of lensed SNe search by means of detecting image multiplicity increases with survey depth. The method becomes more complete than that based on magnification for surveys with depths comparable to or larger than the LSST.

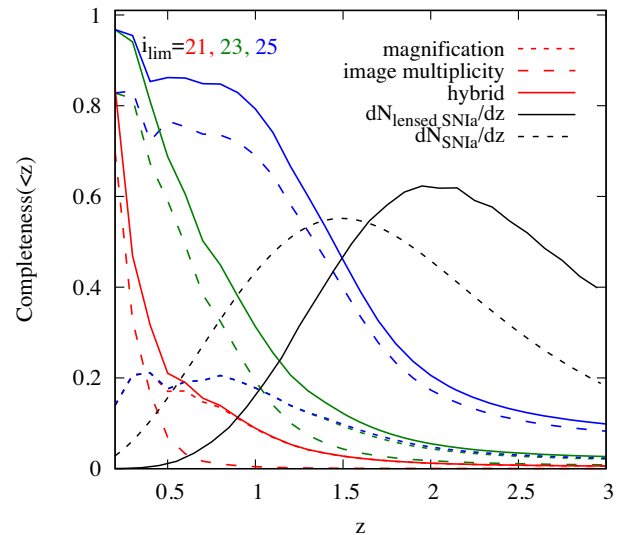


Figure 7. Redshift completeness of lensed type Ia SN candidates found with three different methods, for three limiting magnitudes i_{lim} in the i band. The method based on detecting image multiplicity returns nearly complete redshift samples up to a maximum redshift set by the survey depth. For a reference point, the black curves show redshift distributions of all (non-lensed) or strongly lensed type Ia SNe, both normalized to 1 at $z < 3$.

4.2 Core-collapse supernovae

In Fig. 8, we show the expected detection rates for lensed core-collapse SNe, divided into four subclasses. As for Type Ia SNe, the method of finding lensed SNe by means of detecting highly magnified transients appears to be more effective for shallow surveys, but it is surpassed by the technique based on image multiplicity for deep surveys. The limiting magnitude of comparable

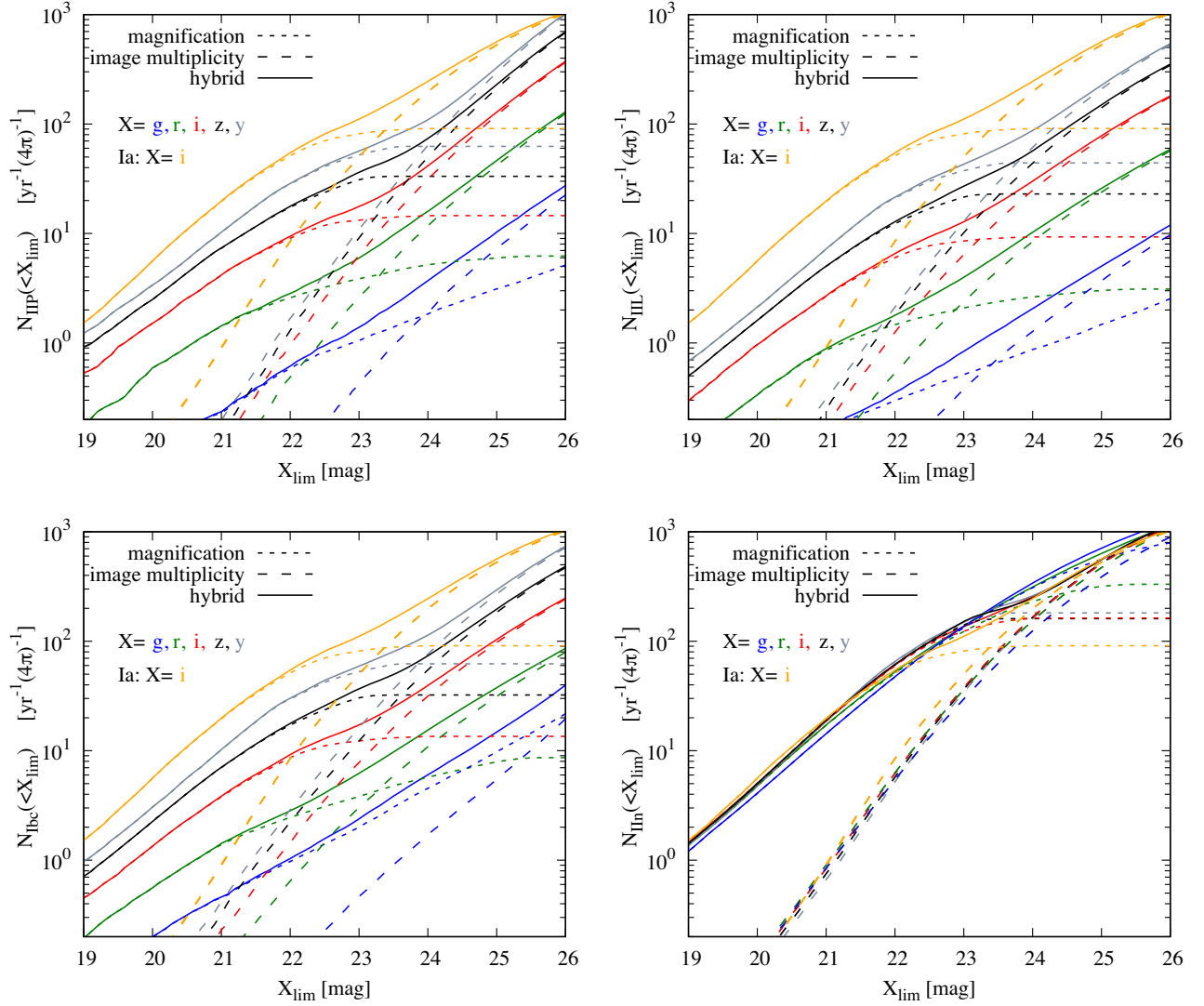


Figure 8. Detection rates of strongly lensed core-collapse SNe (from top left clockwise: IIP, IIL, IIn, and Ib/c) as a function of survey depth in five different bands, in an all-sky search. The long- and short-dashed curves compare the SN yields expected for two different observational strategies based on detecting image multiplicity or highly magnified SNe. The solid curves show the yields for the hybrid method which maximizes detection rates by means of combining both detection criteria. For comparison, the orange curves show the expected rates for lensed type Ia SNe observed in the *i* band.

performances of the two methods depends weakly on the SNe type and filter, and it typically falls within a magnitude range between 23 and 24. The exception in this respect are type IIn SNe for which the magnification-based method appears to be more effective up to as high as 25 mag in the *g* and *r* bands.

The orange curves in Fig. 8 show reference rates for lensed type Ia SNe detectable in the *i* band. Except for type IIn SNe, the discovery rates of lensed core-collapsed SNe are lower than type Ia by a factor of 2–5. A high fraction of luminous type IIn SNe with $M_B < -20$ makes them appreciably easier to detect. Furthermore, the high UV flux of these SNe substantially increases the detection rates in shorter wavelength filters. This considerably reduces the differences between detection rates in the *g* and *y* bands, which is otherwise conspicuous for all other SN types. This effect becomes particularly strong at large limiting magnitudes ($X_{\text{lim}} > 23.5$), where the *g* band appears to be the most effective filter for detecting lensed type IIn SNe via the magnification method.

The total number of detectable lensed core-collapse SNe exceeds that of type Ia, with the primary contribution coming solely from type IIn SNe. The detection rates of lensed SNe of type IIP, IIL, and Ib/c are systematically lower than type Ia.

4.3 Fitting function

For the purpose of future studies exploring the feasibility of using strongly lensed SNe as cosmological and astrophysical probes, we provide a set of simple fitting functions reproducing the computed detection rates. We find that the logarithm of detection rates can be well fitted by a fourth-degree polynomial, i.e.

$$\log_{10} n_{\text{SN}}(< X_{\text{lim}}) = \sum_{i=0}^{i=4} X_i (X_{\text{lim}} - 22.5)^i. \quad (13)$$

Table A1 lists best-fitting parameters for different detection strategies, SN types, and filters.

Table 1. The expected *annual* numbers of discovered lensed supernovae in ongoing or upcoming transient surveys. The method based on image multiplicity is ineffective in case of ZTF and Pan-STARRS, and thus it is omitted in the table. Symbols in parentheses indicate the most effective filter yielding the largest number of detections.

Survey/detection method	Effective area (deg ²)	Type Ia	Type IIP	Type IIL	Type Ib/c	Type IIn
ZTF/magnification	15 000	2.1 (<i>r</i>)	0.37 (<i>r</i>)	0.23 (<i>r</i>)	0.36 (<i>r</i>)	3.8 (<i>r</i>)
Pan-STARRS/magnification	3000	0.9 (<i>i</i>)	0.20 (<i>i</i>)	0.13 (<i>i</i>)	0.20 (<i>i</i>)	0.8 (<i>i</i>)
LSST/magnification	20 000	61 (<i>z</i>)	12.2 (<i>z</i>)	8.7 (<i>y</i>)	12.3 (<i>y</i>)	184 (<i>g</i>)
LSST/image multiplicity	20 000	44 (<i>i</i>)	6.1 (<i>i</i>)	5.5 (<i>i</i>)	6.8 (<i>i</i>)	88 (<i>g</i>)
LSST/hybrid	20 000	89 (<i>iz</i>)	16.3 (<i>iz</i>)	11.9 (<i>iy</i>)	15.8 (<i>iy</i>)	210 (<i>g</i>)

The fitting functions provide accurate approximations to the exact results in a range between $X_{\text{lim}} = 19$ and 26 for all cases. The mean precision given by the root mean square averaged over all cases of filters, SN types, and methods is 0.02 dex.

5 DISCUSSION

The expected detection rates of strongly lensed SNe computed in our work depend on a range of assumptions. The cosmological model, the lens model, and the volumetric rates of type Ia SNe are fairly well constrained by observations and supported by solid theoretical frameworks. On the other hand, the luminosity functions and fractions of different types of SNe, the volumetric rates of core-collapse SNe at high redshifts and the spectral templates of different types of core-collapse SNe (especially type IIn) are less certain and may be a source of additional systematic errors in our estimates. Fig. 4 shows an example of how modifications in the input luminosity function of type Ia SNe can change the expected discovery rates. Bearing in mind that our results may be subject to improvements in the light of future observations, we stress that the predicted discovery rates of lensed SNe presented here reflect the current state of our knowledge on different types of SNe.

In our calculations, we neglect the effect of microlensing. This is a safe assumption, because due to its stochastic nature, microlensing is expected to have a negligible impact on overall predictions of discovery rates of lensed SNe (Goldstein et al. 2018b). However, the effect does perturb light curves independently in every supernova image, giving rise to additional systematic errors in measurements of relative fluxes in the images and time delays (Pierel & Rodney 2019). In our comparison of detection methods we do not consider the problem of possible false positive detections. All methods will be affected by a population of faint quasars increasing stochastically their brightness above the detection limit. Moreover, the magnification method can easily confuse non-lensed superluminous SNe with high-redshift lensed candidates. Quantitative analyses of these effects is worth carrying out in the near future.

In the following, we compare observational strategies for detecting lensed supernovae in the context of ongoing or upcoming transient surveys and the potential of using lensed SNe for cosmological inference.

5.1 Ongoing and upcoming surveys

Strongly lensed SNe will be discovered in appreciable numbers by ongoing and upcoming transient surveys. Table 1 lists the expected discovery rates for the Zwicky Transient Facility (ZTF), LSST, and a hypothetical the Panoramic Survey Telescope and Rapid Response System (Pan-STARRS) survey.

ZTF is an ongoing survey monitoring 15000 deg² in the *g* and *r* bands. For the estimation of discovery rates, we assume that all

candidates will be detected in the most effective filter, i.e. the *r* band. A 5σ limiting magnitude per pointing in this survey is 20.6 (Bellm et al. 2019). As a Pan-STARRS-based survey example, we consider a strategy which is alternative to ZTF. The sky coverage is only 20 per cent of that in ZTF, but in *griz* bands with the same cadence as ZTF. All lensed SNe detectable in this survey would be found in the *i* band for which the survey would reach a 5σ limiting magnitude of 20.6 per pointing. The potentially more effective *z* band would not improve detection rates due to its shallower depth of 20.2. Both ZTF and the Pan-STARRS survey operate in the regime of limiting magnitudes at which the only effective detection technique is the magnification method. Therefore, we omit the rates expected for the image multiplicity and hybrid techniques for them in Table 1.

LSST will cover about 20 000 deg² in 6 *ugrizy* bands every 2–3 weeks with a limiting magnitude of 24 (LSST Science Collaboration et al. 2009, 2017). Precise estimation of discovery rates relies on details of the observational strategy which is yet to be decided. However, reasonable estimates can be obtained based on the following reasoning. A typical redshift of strongly lensed SNe to be discovered by LSST is $z = 1$. This means that the faintest SNe can be detected only within a time window of about 10 d (rest frame) around the peak of their light curve (20 d in the observer frame). In order to satisfy this condition, all detectable SNe should be at least 0.2 mag brighter at the peak than the actual limiting magnitudes of the survey which are (24.5, 24.2, 23.6, 22.8, 22.0) in the *grizy* bands (mean 5σ per pointing; based on LSST collaboration’s simulations, baseline2018a run,² which is the current official reference simulated survey). Then, the expected discovery rate can be found as the maximum rate found for all filters. Since LSST will observe down to limiting magnitudes at which the image multiplicity method becomes effective, we provide rate estimates for all three methods of finding lensed SN candidates. Table 1 also shows the most effective filter (with the highest rate) for different SN types and detection methods.

Pre-LSST surveys may find about five strongly lensed SNe per year, based solely on the magnification method. The most frequent type will be IIn, followed by Ia. Discovery rates will increase by nearly two orders of magnitude for LSST. It is also clear that the magnification method is expected to yield only about two times more discoveries than the image multiplication method. However, both methods will detect lensed SNe at comparable rates when we assume that the measured flux in the magnification methods comes solely from the brightest image (see Fig. 3). Furthermore, keeping in mind that multiply imaged transients do not require follow-up observations confirming their lensing nature (in contrast to highly magnified transients which can be confused with superluminous

²<https://www.lsst.org/scientists/simulations/opsim/opsim-survey-data>

SNe), we conclude that the image multiplicity method will be the most effective technique for finding lensed transients in LSST data.

Lensed SNe discovered by LSST will be typically detected in the i band as a multiply imaged transient and in the y band (or the z band for type Ia and IIP) as a highly magnified transient (except for type IIn which will be discovered primarily in bluer filters). The difference in the effective discovery band can strengthen the complementarity of the two detection techniques. Considering a hybrid method of finding lensed SNe via image multiplicity in the i band and magnification in the y band (or z for Type Ia and IIP), we find that discovery rates in this approach are higher by 30–50 per cent than those based solely on magnification.

Except for type IIP SNe, our discovery rates estimated for ZTF and LSST based on the magnification method agree fairly well with analogous predictions obtained by Goldstein et al. (2018a). Adopting the same detection conditions and survey parameters for LSST, we also recover fairly closely the rates estimated by Oguri & Marshall (2010), with the total number of lensed Type Ia and core-collapse SNe to be discovered by LSST of 32 and 36. These rates are lower by a factor of >10 than those listed in Table 3 and obtained by Goldstein et al. (2018a). These differences can be fully accounted for to the stricter detection criteria adopted by Oguri & Marshall (2010), i.e. an effective limiting magnitude of 22.6 in the i band (in order to sample light curves at minimum depth of 0.7 mag around the peak) and an effective survey time of 2.5 yr (accounting for seasonal changes of the surveyed area), and do not signal discrepancies in the basic methodologies in the independent approaches to estimating detection rates. It is worth mentioning that more restrictive selection criteria than those proposed by Oguri & Marshall (2010) are required for obtaining high-quality measurements of gravitational time delays. In particular, a minimum precision of 5 per cent and an accuracy of 1 per cent in the time delay measurements (if based solely on LSST observations) would reduce the number of lensed type Ia SNe to about 1 per year (Huber et al. 2019). This rate can be increased by a factor of 2–16 by employing other instruments for follow-up observations.

5.2 Observed fractions of supernova types

Fig. 9 shows predicted fractions of different types of SNe in representative samples of gravitationally lensed SNe expected in transient surveys with a range of limiting magnitudes between 19 and 26.

The observed fractions depend quite weakly on limiting magnitude. The most noticeable trend occurs for type IIP, IIL, and Ibc at large limiting magnitudes for the image multiplicity method. The highest fractions of these supernovae are expected for extremely shallow or deep surveys.

Type Ia and IIn SNe clearly dominate detections, with fractions of about 30 per cent each. The prevalence of type IIn SNe becomes even stronger Ia when one includes detections in the g band, the most efficient filter for observing type IIn SNe. We emphasize that the high relative discovery rates of type IIn SNe rely quite strongly on the adopted spectral templates which in turn depend on the extinction correction performed in the analysis of the observational data used here (see Di Carlo et al. 2002).

Nevertheless, the high predicted relative detection rates of lensed type IIn SNe is intriguing. The rates and luminosity distribution of type IIn supernovae at high redshift are quite uncertain, theoretically because of their wide range of possible progenitors, including very massive stars in the tail of the initial mass function (e.g. Gal-Yam & Leonard 2009; Smith 2014; Thöne et al. 2017) and observationally,

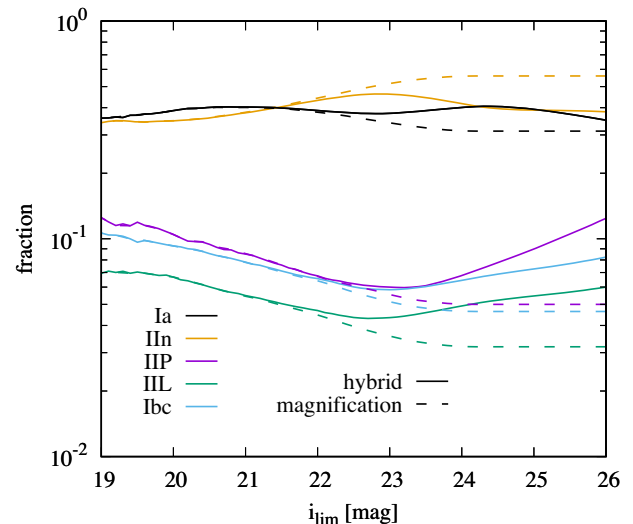


Figure 9. Fractions of different SN types in samples of gravitationally lensed SNe detected in transient surveys with limiting magnitude i_{lim} in the i band. Gravitationally lensed SNe are detected via magnification (dashed curves) or using the hybrid method (solid curves).

because of their diverse photometric properties (e.g. Taddia et al. 2013; Richardson et al. 2014b; Cappellaro et al. 2015). Fortunately, lensed type IIn SNe can readily be distinguished from other SNe due to their narrow (and hence high spectroscopic signal-to-noise ratio) Balmer emission lines. Hence, observations of lensed IIn could provide unique insights into their intrinsic properties at high redshift.

5.3 Discovery space

The detection methods considered in this study may also lead to differences in the phase space of lensing configurations. Fig. 10 shows the distributions of basic lensing parameters of lensed type Ia SNe as a function of limiting i -band magnitude. The green contours show 10-quantiles of the distributions expected for the hybrid method. The purple and orange curves show the median and a range containing 80 per cent of the cases for the magnification and image multiplicity techniques, respectively. We omit results for the image multiplication technique at limiting magnitudes lower than $i_{\text{lim}} = 21.5$ where the method is far less competitive, with the potential discovery rate smaller than 10 per cent of that of the magnification technique. Fig. 10 also shows the fractions of the different image configurations with two (doubles), three (cusps), and four images (quads).

Gravitationally lensed supernovae to be found in ongoing pre-LSST shallow surveys will be extremely magnified. For a limiting magnitude of 20.6 (depth of ZTF), the expected mean magnification is 20 and a 10 per cent tail of the distribution includes cases with magnifications exceeding 100. For shallower surveys, the expected magnification become substantially higher with the mean reaching $\mu = 100$ at $i_{\text{lim}} = 19.5$.

The expected lensing properties of lensed SNe detected via magnification pose a challenge to using them as cosmological probes. In particular, the typical time delays for lensed SNe found in pre-LSST surveys are below 10 d and typical image separations will hardly exceed the arcsecond scale. Fig. 10 demonstrates that LSST or deeper surveys – with typical time delays always below 10 d – can hardly mitigate this problem. In this respect, the image

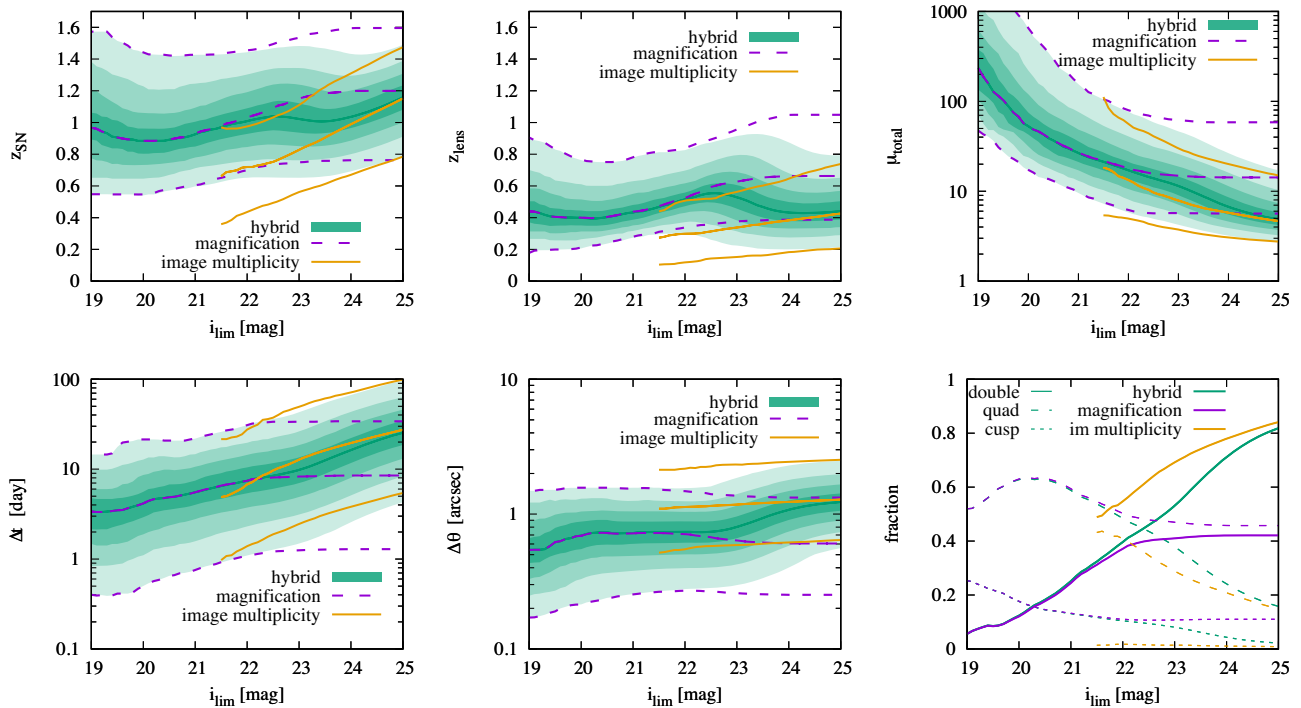


Figure 10. Discovery space of gravitationally lensed type Ia SNe detected with different methods in a single-filter survey with depth i_{lim} in the i band. The panels show distributions of supernova redshift z_{SN} , lens redshift z_{lens} , total magnification μ_{total} , gravitational time delay averaged over all image pairs $\langle \Delta t \rangle$ and image separation averaged over all image pairs $\langle \Delta \theta \rangle$. The green contours show 10-quantiles of the distributions for supernova samples produced by the hybrid method. The purple and orange curves show the median and 80-percent probability range of probability distributions for the magnification and image multiplicity methods, respectively. The results for the image multiplicity are shown only for detection rates larger than 10 per cent of the corresponding detection rates for the magnification method. The bottom right panel shows fractions of different lensing configurations with two images (doubles), three images (cusps), or four images (quads).

multiplicity method appears to be more promising. When applied to LSST-like surveys ($i_{\text{lim}} = 23.5$), the method is expected to find lensed SNe with the mean time delay of 20 d (and a 10 per cent tail of the distribution with time delays at least 60 d) and typical image separations larger than 1 arcsec. Undoubtedly, this increases the potential for using lensed SNe to place robust cosmological constraints.

Time delays and image separations are not the only differences between the populations of lensed SNe found via magnification and image multiplicity. We also find that the image multiplicity method is more sensitive to SNe and lens galaxies at lower redshifts. There is also a clear difference in terms of image configuration. A much larger fraction of lensed supernovae found via image multiplicity are doubles, whereas for the magnification methods the numbers of quads and doubles are comparable. Unsurprisingly, both methods exhibit an increasing (decreasing) trend in the fraction of doubles (quads) with increasing limiting magnitude. The fraction of cups is at the sub-percent level for the image magnification methods, whereas it reaches a 10-per cent level for the magnification technique.

In the context of discussing the future phase space of lensing configurations, it is interesting to consider the case of the gravitationally lensed sn iPTF16geu. The sn was discovered in a relatively shallow survey. In this respect, its high magnification of $\mu_{\text{total}} \sim 50$ is not surprising. However, the observed magnification turns out to be at odds with the theoretical expectations when the redshift of the sn is taken into account (More et al. 2017; Goldstein et al. 2018a). In order to address this tension, we compute 2D credibility

contours for redshifts and gravitational magnifications of all lensed SNe detectable in a transient survey equivalent to the iPTF. As a nominal depth of the survey, we consider either 20.5 or 20.0 in the r band. The latter is a more appropriate choice when one requires good observations of light curves around the peak (More et al. 2017). The SN was discovered as a peculiarly bright, initially unresolved, transient; therefore, it is justified to employ the magnification method as an effective approach to finding lensed transients in the iPTF survey. As shown in Fig. 11, the tension between iPTF16geu and theoretical predictions is at a quite modest level of 2σ . We conclude that the peculiar lensing configuration of iPTF16geu can be simply a statistical fluke. However, the flux ratio anomalies between observed brightness of the images and the best-fitting lens model pose a serious problem because the discrepancy seems too large to be ascribed to microlensing (Yahalom, Schechter & Wambsganss 2017).

6 SUMMARY AND CONCLUSIONS

We have compared different observational strategies for detecting gravitationally lensed SNe in massive transient surveys. The strategies rely on finding multiply imaged transients or highly magnified SNe (deduced via comparing observed magnitudes to fiducial magnitudes of a type Ia SN located in the apparent host galaxy). Adopting state-of-the-art models of lens galaxies constrained by the SDSS data and the standard cosmological Λ CDM mode, we have calculated detection rates for each method in five *grizy* bands for the main SN classes including: type Ia, core-collapse SNe types IIP,

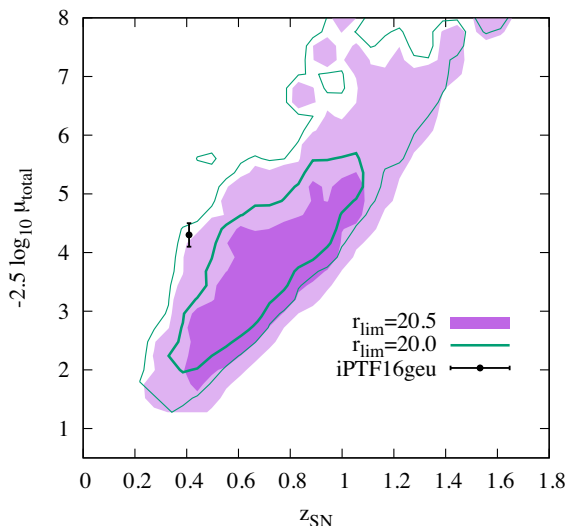


Figure 11. The expected distribution of the total magnification and redshift (in the form of 1σ and 2σ credibility contours) of lensed SNe detectable in the iPTF survey with limiting magnitude r_{lim} in the r band, compared to the measured parameters of observed gravitationally lensed SNe iPTF16geu. The observed SNe lies well within a 2σ contour.

III, Ibc, and IIc. We provide simple fitting functions approximating the computed rates.

We find that detecting lensed supernovae as strongly magnified transients is the only effective detection method working for shallow pre-LSST surveys with limiting magnitudes smaller than 22. However, the expected yields saturate at limiting magnitudes of about 23.0–23.5 (depending on SN type and filter) where lensed supernovae are more likely to be fainter than a fiducial type Ia SN in the apparent host galaxies (lens galaxy). At this limiting magnitude, the magnification and image multiplicity method yield comparable numbers of lensed SNe. SNe found by the two methods are to a large extent independent; therefore, a noticeable improvement of discovery rates can be achieved by combining the two methods. The resulting hybrid method increases the yields by 50 per cent at limiting magnitudes corresponding to comparable rates expected for the two primary methods. For larger limiting magnitudes $\gtrsim 23.5$, the image multiplicity method completely surpasses the performance of the magnification technique.

Detection rates depend strongly on filter. Except for type IIc, discovery rates decrease with decreasing effective wavelength. An inverse trend found for type IIc SNe results from the presence of strong UV flux and a relatively higher incidence of luminous SNe with $M_B < -20$. In the overall counts of gravitationally lensed SNe, type IIc will be the most common class followed by type Ia, regardless of the adopted detection method. The rates are dominated by intrinsically bright SNe; therefore, the robustness of our predictions rely on accurate modelling of high-luminosity tails of the SN luminosity functions, currently approximated by Gaussian distributions.

Revisiting the initial comparison between the image multiplicity and magnification methods made by Goldstein & Nugent (2017), we find that detecting lensed SNe via image multiplicity is as efficient as the magnification method at the limiting magnitudes of LSST and it surpasses the latter for deeper surveys. Moreover, strongly lensed SNe found via image multiplicity are also characterized by longer time delays and larger image separations than systems found via magnification. This makes the image multiplicity method a

more appealing observational strategy for LSST when considering the potential of using lensed SNe as cosmological probes. It is also worth mentioning that the image multiplicity approach does not rely on follow-up observations and it can be naturally applied to self-contained massive surveys without auxiliary imaging observations. In contrast, candidates for lensed SNe selected via magnification naturally require follow-up observations to confirm their the lensing nature.

We estimate that ZTF with a depth of 20.6 in the r band will detect 1.9 type Ia 4.1 core-collapse (primarily IIc) lensed SNe per year. Analogous computations for LSST yield 44 type Ia and 106 core-collapse (primarily IIc) lensed SNe per year, detected via image multiplicity. The hybrid method will allow to increase these rates to 89 and 254 detections per year for type Ia and core collapse, respectively. Core-collapse lensed SNe will be dominated by type IIc with relative fraction of 80 per cent.

ACKNOWLEDGEMENTS

We are highly indebted to the referee, Prasenjit Saha, for his insightful comments and helpful suggestions. This work was supported by a VILLUM FONDEN Investigator grant to JH (project number 16599).

REFERENCES

- Andersen P., Hjorth J., 2018, *MNRAS*, 480, 68
 Anderson J. P. et al., 2014, *ApJ*, 786, 67
 Barbary K. et al., 2012, *ApJ*, 745, 31
 Belczynski K., Bulik T., Ruiter A. J., 2005, *ApJ*, 629, 915
 Bellm E. C. et al., 2019, *PASP*, 131, 018002
 Bezanson R. et al., 2011, *ApJ*, 737, L31
 Blanc G. et al., 2004, *A&A*, 423, 881
 Botticella M. T. et al., 2008, *A&A*, 479, 49
 Cano Z., Selsing J., Hjorth J., de Ugarte Postigo A., Christensen L., Gall C., Kann D. A., 2018, *MNRAS*, 473, 4257
 Cappellaro E. et al., 2015, *A&A*, 584, A62
 Cappellaro E., Evans R., Turatto M., 1999, *A&A*, 351, 459
 Castro T., Quartin M., Giocoli C., Borgani S., Dolag K., 2018, *MNRAS*, 478, 1305
 Chae K.-H., 2003, *MNRAS*, 346, 746
 Chen W. et al., 2019, preprint ([arXiv:1902.05510](https://arxiv.org/abs/1902.05510))
 Choi Y.-Y., Park C., Vogeley M. S., 2007, *ApJ*, 658, 884
 Dahlen T., Strolger L.-G., Riess A. G., 2008, *ApJ*, 681, 462
 Di Carlo E. et al., 2002, *ApJ*, 573, 144
 Diego J. M., 2018, *A&A*, 625, 484
 Dilday B. et al., 2008, *ApJ*, 682, 262
 Dilday B. et al., 2010, *ApJ*, 713, 1026
 Gal-Yam A., Leonard D. C., 2009, *Nature*, 458, 865
 Gilliland R. L., Nugent P. E., Phillips M. M., 1999, *ApJ*, 521, 30
 Goldstein D. A., Nugent P. E., 2017, *ApJ*, 834, L5
 Goldstein D. A., Nugent P. E., Goobar A., 2018a, preprint ([arXiv:1809.10147](https://arxiv.org/abs/1809.10147))
 Goldstein D. A., Nugent P. E., Kasen D. N., Collett T. E., 2018b, *ApJ*, 855, 22
 Goobar A. et al., 2017, *Science*, 356, 291
 Graur O. et al., 2011, *MNRAS*, 417, 916
 Graur O. et al., 2014, *ApJ*, 783, 28
 Graur O., Maoz D., 2013, *MNRAS*, 430, 1746
 Graur O., Bianco F. B., Modjaz M., Shivvers I., Filippenko A. V., Li W., Smith N., 2017, *ApJ*, 837, 121
 Grillo C. et al., 2018, *ApJ*, 860, 94
 Hardin D. et al., 2000, *A&A*, 362, 419
 Holder G. P., Schechter P. L., 2003, *ApJ*, 589, 688

- Horesh A., Poznanski D., Ofek E. O., Maoz D., 2008, *MNRAS*, 389, 1871
- Huber S. et al., 2019, preprint (arXiv:1903.00510)
- Kaurov A. A., Dai L., Venumadhav T., Miralda-Escudé J., Frye B., 2019, preprint (arXiv:1902.10090)
- Keeton C. R., Kochanek C. S., Seljak U., 1997, *ApJ*, 482, 604
- Kelly P. L. et al., 2015, *Science*, 347, 1123
- Kelly P. L. et al., 2016, *ApJ*, 831, 205
- Kelly P. L. et al., 2018, *Nat. Astron.*, 2, 334
- Kochanek C. S., 1991, *ApJ*, 373, 354
- Kolatt T. S., Bartelmann M., 1998, *MNRAS*, 296, 763
- Kormann R., Schneider P., Bartelmann M., 1994, *A&A*, 284, 285
- Levan A. et al., 2005, *ApJ*, 624, 880
- Li W. et al., 2011, *MNRAS*, 412, 1441
- LSST Science Collaboration et al., 2009, preprint (arXiv:0912.0201)
- LSST Science Collaboration et al., 2017, preprint (arXiv:1708.04058)
- Madau P., Dickinson M., 2014, *ARA&A*, 52, 415
- Maoz D., Mannucci F., 2012, *PASA*, 29, 447
- Melinder J. et al., 2012, *A&A*, 545, A96
- Mitchell J. L., Keeton C. R., Frieman J. A., Sheth R. K., 2005, *ApJ*, 622, 81
- Montero-Dorta A. D., Bolton A. S., Shu Y., 2017, *MNRAS*, 468, 47
- More A., Suyu S. H., Oguri M., More S., Lee C.-H., 2017, *ApJ*, 835, L25
- Nugent P., Kim A., Perlmutter S., 2002, *PASP*, 114, 803
- Oguri M. et al., 2008, *AJ*, 135, 512
- Oguri M., 2010, *PASJ*, 62, 1017
- Oguri M., Kawano Y., 2003, *MNRAS*, 338, L25
- Oguri M., Marshall P. J., 2010, *MNRAS*, 405, 2579
- Pain R. et al., 2002, *ApJ*, 577, 120
- Perrett K. et al., 2012, *AJ*, 144, 59
- Pierel J. R., Rodney S. A., 2019, *ApJ*, 876, 107
- Quimby R. M. et al., 2014, *Science*, 344, 396
- Refsdal S., 1964, *MNRAS*, 128, 307
- Richardson D., Jenkins R. L., III, Wright J., Maddox L., 2014a, *AJ*, 147, 118
- Richardson D., Jenkins R. L., III, Wright J., Maddox L., 2014b, *AJ*, 147, 118
- Rodney S. A. et al., 2014, *AJ*, 148, 13
- Rodney S. A. et al., 2015, *ApJ*, 811, 70
- Rodney S. A. et al., 2016, *ApJ*, 820, 50
- Rodney S. A. et al., 2018, *Nat. Astron.*, 2, 324
- Rodney S. A., Tonry J. L., 2010, *ApJ*, 723, 47
- Schneider P., Sluse D., 2014, *A&A*, 564, A103
- Smith N., 2014, *ARA&A*, 52, 487
- Taddia F. et al., 2013, *A&A*, 555, A10
- Thöne C. C. et al., 2017, *A&A*, 599, A129
- Tonry J. L. et al., 2003, *ApJ*, 594, 1
- Vega-Ferrero J., Diego J. M., Miranda V., Bernstein G. M., 2018, *ApJ*, 853, L31
- Witt H. J., Mao S., 1997, *MNRAS*, 291, 211
- Yahalom D. A., Schechter P. L., Wambsganss J., 2017, preprint (arXiv:1711.07919)

APPENDIX A: PARAMETERS OF FITTING FUNCTION

Table A1. Best-fitting parameters of a polynomial function approximating the computed rates of detecting strongly lensed SNe, for different detection methods and bandpass filters. The fitting function is given by equation (13) and the rates are in units of $\text{yr}^{-1} (4\pi)^{-1}$ (yields from a full-sky survey per year).

Method	SN type	Bandpass	X_0	X_1	X_2	X_3	X_4
Magnification	Ia	<i>g</i>	0.72036	0.24009	−0.03900	0.00477	0.00104
Magnification	Ia	<i>r</i>	1.33862	0.19880	−0.04735	0.00450	−0.00012
Magnification	Ia	<i>i</i>	1.83059	0.21667	−0.09311	0.00355	0.00255
Magnification	Ia	<i>z</i>	2.07615	0.25577	−0.10111	0.00216	0.00285
Magnification	Ia	<i>y</i>	2.23439	0.29536	−0.10980	0.00041	0.00343
Multiple images	Ia	<i>g</i>	0.48173	0.61185	−0.06134	0.00563	−0.00097
Multiple images	Ia	<i>r</i>	1.07923	0.67684	−0.07377	0.00196	−0.00009
Multiple images	Ia	<i>i</i>	1.33432	0.80388	−0.09728	−0.01051	0.00351
Multiple images	Ia	<i>z</i>	1.38904	0.88393	−0.08518	−0.01878	0.00392
Multiple images	Ia	<i>y</i>	1.38537	0.94450	−0.07931	−0.02503	0.00464
Hybrid	Ia	<i>g</i>	0.88408	0.37177	−0.00971	0.00149	−0.00033
Hybrid	Ia	<i>r</i>	1.47731	0.36007	0.00447	0.00321	−0.00195
Hybrid	Ia	<i>i</i>	1.89609	0.35927	−0.02158	0.00505	−0.00031
Hybrid	Ia	<i>z</i>	2.10720	0.37109	−0.03153	0.00530	0.00018
Hybrid	Ia	<i>y</i>	2.24285	0.38345	−0.04630	0.00507	0.00118
Magnification	IIP	<i>g</i>	−0.09803	0.30353	−0.03839	−0.00170	0.00210
Magnification	IIP	<i>r</i>	0.51297	0.18132	−0.03835	0.00365	−0.00023
Magnification	IIP	<i>i</i>	1.05567	0.17664	−0.07500	0.00283	0.00206
Magnification	IIP	<i>z</i>	1.37635	0.22296	−0.08338	0.00011	0.00265
Magnification	IIP	<i>y</i>	1.60361	0.26657	−0.09178	−0.00201	0.00324
Multiple image	IIP	<i>g</i>	−0.73742	0.74209	−0.02966	−0.00791	0.00130
Multiple image	IIP	<i>r</i>	0.05035	0.79421	−0.05724	−0.01589	0.00452
Multiple image	IIP	<i>i</i>	0.39685	0.85468	−0.06020	−0.01743	0.00460
Multiple image	IIP	<i>z</i>	0.53709	0.87378	−0.04444	−0.01662	0.00342
Multiple image	IIP	<i>y</i>	0.62664	0.86039	−0.03253	−0.01300	0.00225
Hybrid	IIP	<i>g</i>	−0.03277	0.39937	0.00269	−0.00081	0.00066
Hybrid	IIP	<i>r</i>	0.61623	0.33920	0.02793	0.00642	−0.00203
Hybrid	IIP	<i>i</i>	1.10586	0.32201	0.00987	0.00839	−0.00064
Hybrid	IIP	<i>z</i>	1.39204	0.32922	−0.00632	0.00811	0.00059
Hybrid	IIP	<i>y</i>	1.60046	0.33684	−0.02764	0.00781	0.00209

Table A1 – continued

Method	SN type	Bandpass	X_0	X_1	X_2	X_3	X_4
Magnification	IIL	<i>g</i>	−0.40183	0.23634	−0.01517	0.00582	−0.00057
Magnification	IIL	<i>r</i>	0.25718	0.15857	−0.03946	0.00435	−0.00008
Magnification	IIL	<i>i</i>	0.86956	0.17352	−0.07717	0.00352	0.00206
Magnification	IIL	<i>z</i>	1.22347	0.22128	−0.08761	0.00140	0.00264
Magnification	IIL	<i>y</i>	1.46877	0.26402	−0.09947	−0.00036	0.00340
Multiple image	IIL	<i>g</i>	−0.74372	0.65666	−0.05661	−0.00358	0.00195
Multiple image	IIL	<i>r</i>	0.07288	0.66921	−0.06623	−0.00301	0.00203
Multiple image	IIL	<i>i</i>	0.47375	0.72861	−0.07291	−0.00444	0.00220
Multiple image	IIL	<i>z</i>	0.65237	0.77378	−0.06863	−0.00711	0.00228
Multiple image	IIL	<i>y</i>	0.78459	0.79863	−0.05759	−0.00825	0.00117
Hybrid	IIL	<i>g</i>	−0.26604	0.36248	0.01242	0.00311	−0.00151
Hybrid	IIL	<i>r</i>	0.41663	0.35667	0.01112	0.00232	−0.00097
Hybrid	IIL	<i>i</i>	0.95985	0.34048	0.00086	0.00553	−0.00076
Hybrid	IIL	<i>z</i>	1.26577	0.34858	−0.01301	0.00577	0.00010
Hybrid	IIL	<i>y</i>	1.48178	0.35631	−0.03247	0.00597	0.00141
Magnification	Ibc	<i>g</i>	0.14709	0.31974	0.00689	0.00305	−0.00104
Magnification	Ibc	<i>r</i>	0.49563	0.20613	−0.02187	0.00285	−0.00080
Magnification	Ibc	<i>i</i>	1.02766	0.17760	−0.07830	0.00321	0.00219
Magnification	Ibc	<i>z</i>	1.37074	0.22244	−0.08762	0.00128	0.00264
Magnification	Ibc	<i>y</i>	1.61716	0.26280	−0.09812	−0.00027	0.00329
Multiple images	Ibc	<i>g</i>	−0.67826	0.63296	−0.01858	−0.00064	−0.00025
Multiple images	Ibc	<i>r</i>	0.16955	0.68416	−0.07132	−0.00334	0.00255
Multiple images	Ibc	<i>i</i>	0.55571	0.74754	−0.07414	−0.00661	0.00290
Multiple images	Ibc	<i>z</i>	0.73853	0.75590	−0.05557	−0.00484	0.00125
Multiple images	Ibc	<i>y</i>	0.85114	0.77360	−0.05053	−0.00659	0.00142
Hybrid	Ibc	<i>g</i>	0.19634	0.35951	0.01349	0.00263	−0.00104
Hybrid	Ibc	<i>r</i>	0.62451	0.34332	0.01745	0.00303	−0.00160
Hybrid	Ibc	<i>i</i>	1.09885	0.32867	−0.00133	0.00634	−0.00050
Hybrid	Ibc	<i>z</i>	1.40103	0.33547	−0.01531	0.00681	0.00035
Hybrid	Ibc	<i>y</i>	1.62488	0.34237	−0.03615	0.00692	0.00172
Magnification	IIn	<i>g</i>	1.90814	0.45380	−0.03934	−0.00427	0.00045
Magnification	IIn	<i>r</i>	1.91461	0.38611	−0.05516	−0.00382	0.00061
Magnification	IIn	<i>i</i>	1.95587	0.31645	−0.10087	−0.00210	0.00325
Magnification	IIn	<i>z</i>	1.98209	0.31814	−0.10942	−0.00231	0.00377
Magnification	IIn	<i>y</i>	2.01341	0.33552	−0.10991	−0.00248	0.00357
Multiple images	IIn	<i>g</i>	1.11411	0.72917	−0.04473	−0.00435	0.00007
Multiple images	IIn	<i>r</i>	1.18910	0.75405	−0.05117	−0.00637	0.00056
Multiple images	IIn	<i>i</i>	1.19611	0.78006	−0.05496	−0.00828	0.00096
Multiple images	IIn	<i>z</i>	1.17156	0.79957	−0.05529	−0.00965	0.00115
Multiple images	IIn	<i>y</i>	1.13596	0.81564	−0.05541	−0.01082	0.00136
Hybrid	IIn	<i>g</i>	1.91431	0.46530	−0.03247	−0.00292	0.00050
Hybrid	IIn	<i>r</i>	1.94418	0.42431	−0.03745	−0.00056	0.00074
Hybrid	IIn	<i>i</i>	1.96332	0.37749	−0.05314	0.00379	0.00213
Hybrid	IIn	<i>z</i>	1.98247	0.37635	−0.05987	0.00410	0.00260
Hybrid	IIn	<i>y</i>	2.00122	0.38171	−0.06689	0.00395	0.00299

This paper has been typeset from a \LaTeX file prepared by the author.